

**Correction of secondary fluorescence across phase boundaries in electron probe microanalysis of mineral inclusions**

Xavier Llovet<sup>1,\*</sup>, Joaquín A. Proenza<sup>2</sup>, Núria Pujol-Solà<sup>2</sup>, Júlia Farré-de-Pablo<sup>2</sup>, Marc Campeny<sup>3</sup>

<sup>1</sup> Centres Científics i Tecnològics, Universitat de Barcelona. Lluís Solé i Sabarís, 1-3. 08028 Barcelona, Spain

<sup>2</sup> Departament de Mineralogia, Petrologia i Geologia Aplicada, Universitat de Barcelona. Martí i Franqués, s/n. 08028 Barcelona, Spain

<sup>3</sup> Departament de Mineralogia, Museu de Ciències Naturals de Barcelona, Passeig Picasso s/n, 08003 Barcelona, Spain

\*Corresponding author. E-mail: xavier@ccit.ub.edu

**Abstract**

One of the limiting factors for the analysis of minor elements in multiphase materials by electron probe microanalysis is the effect of secondary fluorescence (SF), which is not accounted for by matrix corrections. Although the apparent concentration due to SF can be calculated numerically or measured experimentally, detailed investigations of this effect for fine-grained materials are scarce. In this work, we use the Monte Carlo simulation program PENEPA to examine and correct the effect of SF affecting micron-sized mineral inclusions hosted by other minerals. A concentration profile across an olivine  $[(\text{Mg,Fe})_2\text{SiO}_4]$  inclusion in chromite ( $\text{Fe}^{2+}\text{Cr}_2\text{O}_4$ ) is measured and used to assess the reliability of calculations, where different boundary geometries are examined. Three examples of application are presented, which include the determination of Cr in olivine and serpentine  $[\text{Mg}_3\text{Si}_2\text{O}_5(\text{OH})_4]$  inclusions hosted by chromite, and of Fe in quartz ( $\text{SiO}_2$ ) inclusions hosted by almandine garnet ( $\text{Fe}_3\text{Al}_2\text{Si}_3\text{O}_{12}$ ). Our results show that neglecting SF leads to concentrations that are overestimated by  $\sim 0.1$ - $0.8$  wt.%, depending on inclusion size. In addition, assuming a straight boundary yields to an underestimation of SF effects by a factor of  $\sim 2$ - $4$ .

Because its long-range nature, SF severely compromises trace-element analyses even for phases as large as 1 mm in size.

## 1 Introduction

Electron probe microanalysis (EPMA) is an analytical technique widely used for the analysis of rock-forming minerals. The spatial resolution of EPMA is primarily governed by the interaction volume of incident electrons inside the specimen, which is typically of a few microns across depending on beam energy and material. Thus, EPMA is ideally suited for the analysis of mineral phases with dimensions greater than a few microns across such as mineral inclusions embedded in other minerals. However, the range of X-rays generated by the electron beam exceeds that of incident electrons by more than one order of magnitude and, therefore, primary X-rays may travel across the sample and generate secondary fluorescence (SF) far away from the analyzed phase. The contribution of SF across phase boundaries, which acts to enhance the element's concentration, is not accounted for by matrix correction methods since they assume that the sample is chemically homogeneous. Although the effect of SF is small and can generally be neglected, analytical errors may be important when analyzing for a minor/trace element in a phase surrounded by another phase that contains a large abundance of the element of interest. SF may also arise due to calibrating in large standards compared to analyzing small micro-volumes, as fluorescence at a distance from the beam will contribute more substantially to the standard emission.

The effect of SF across phase boundaries has been known for decades (Reed & Long, 1963) and its potential analytical errors have been discussed in the literature. Smith (1966) stated that "even though the microprobe technique permits spot analyses, accurate data will be hard to obtain because of possible fluorescence excitation outside the region of primary excitation". Yet, the incorporation of SF corrections into the matrix correction procedures has remained elusive and errors due to SF have often been overlooked. An example is the study by Sato and Santosh (2007), where temperatures obtained from EPMA analyses in quartz adjacent to rutile ( $\text{TiO}_2$ ) were overestimated due to uncorrected SF effects (Zhang et al., 2019).

A solution to account for SF is to extract the mineral of interest and analyze it separately (Hermann et al., 2005). For example, Köhler & Brey (1990) separated olivine  $[(\text{Mg,Fe})_2\text{SiO}_4]$  grains to avoid SF when calibrating an olivine-clinopyroxene  $[\text{CaMgSi}_2\text{O}_6]$  geothermometer. Likewise, Brenan (2003) extracted olivine grains immersed in a Ni-rich sulfide melt in order to avoid fluorescence from the melt. However, separating grains is tedious and not always possible, thus the possibility of obtaining valuable data from fine-grained samples may be lost. Moreover, the real power of EPMA is the in-situ nature, particularly in geologic applications where the context is very important.

Another solution is to prepare cold-pressed mineral couples and to step across the boundary to measure SF experimentally. Longhi et al. (1976) made measurements on plagioclase  $[(\text{Na,Ca})(\text{Si,Al})_3\text{O}_8]$  in contact with glass to estimate the apparent Fe content due to SF. Adams and Bishop (1986) estimated the apparent Ca contents in olivine adjacent to clinopyroxene by measuring an olivine-clinopyroxene couple. Watson (1979) measured the apparent Ca concentration in Ca-free forsterite ( $\text{Mg}_2\text{SiO}_4$ ) adjacent to glass and concluded that olivine crystals smaller than 30  $\mu\text{m}$  were not suitable for analysis. Jurewicz & Watson (1988) obtained apparent concentration profiles in olivine adjacent to melt. McKay (1986) measured the apparent Sm concentration of a rare-earth element (REE)-free olivine adjacent to REE-containing glass, observing that it extends over 100  $\mu\text{m}$  in olivine. Capobianco & Amelin (1994) observed directional effects, which depended on the orientation of the sample inside the microprobe, when measuring SF profiles in several metal-silicate couples. Dalton & Lane (1996) made systematic measurements of apparent Ca concentrations in olivine in contact with different Ca-containing minerals, which have been later used to assess the accuracy of SF calculations (Llovet et al., 2012; Ritchie, 2017). Other measurements include the determination of Ti in garnet  $[(\text{Fe,Mn})_3\text{Al}_2\text{Si}_3\text{O}_{12}]$  in contact with ilmenite  $[(\text{Fe,Mn})\text{TiO}_3]$  (Feenstra & Engi, 1998), of Fe in plagioclase next to glass and fayalite ( $\text{Fe}_2\text{SiO}_4$ ) (Sugawara, 2001), and of Ti in San Carlos olivine and periclase ( $\text{MgO}$ ) adjacent to rutile (Hermann et al., 2005). Borisova et al. (2018) presented new SF measurements for different mineral-mineral and mineral-glass couples and estimated the errors that would be made in applying the associated geothermometers without correcting for SF. More recently, Zhang et al. (2018) measured the apparent contents of Ni in olivine adjacent to Ni-rich quenched sulfide melt.

The effect of SF can also be calculated theoretically (Hénoc et al., 1969; Bastin et al., 1983; Llovet et al., 2012). The simplest approach is to assume that the sample is an undiffused couple, i.e., it consists of two semi-infinite media separated by a plane boundary perpendicular to the sample surface. The calculation of SF across the interface can be then performed semi-analytically. Llovet et al. (2012) developed the computer code FANAL, which calculates semi-analytically SF effects in undiffused couples. This code has been shown to accurately predict SF effects when the samples match the geometry assumed in the model (Llovet et al., 2012; Borisova et al., 2018) and has been used to assess SF effects in a variety of samples (Goodrich et al., 2014; Ackerson et al., 2017; Singerling & Brearley, 2018; Zhang et al., 2018; D'Souza et al., 2020). For more complicated geometries such as particles, inclusions or lamellae, calculations are difficult and have been rarely addressed. One exception is the work of Bastin et al. (1983), who developed a method for calculating SF in hemisphere inclusions, but the contribution of bremsstrahlung photons was ignored. We will see later that this contribution is by no means negligible.

While the use of experimental data or semi-analytical calculations obtained for undiffused couples is suitable for correcting SF in large crystals, its application to fine-grain minerals is limited

(D'Souza et al., 2020). On that account, it is no surprise that FANAL would overestimate the Ti enhancement produced by a small rutile inclusion in a host garnet (Ackerson et al., 2017). On the other hand, SF measurements on inclusions or fine-grained minerals are rare (Robinson et al., 1998; Jercinovic et al., 2008; Zhao et al., 2015).

Myklebust & Newbury (1995) calculated SF effects by using the Monte Carlo simulation method of particle transport. This method consists in numerically generating the particle trajectories within the material, which are viewed as a sequence of “free” flights that end with an interaction event (where the particle changes its direction of movement, loses energy and may generate secondary particles), and quantities of interest are obtained by averaging over a large number of trajectories. The advantage of the Monte Carlo method is that it can be applied to samples with relatively complex geometries (see e.g., Jennings et al., 2019a, 2019b). Its main drawback is that results are affected by statistical uncertainties, which in principle can only be reduced by increasing the simulation time, but recent progress in variance-reduction techniques along with the increasing availability of fast computers have enhanced the attractiveness of this method for SF calculations (Llovet & Salvat, 2017; Ritchie, 2017; Yuan et al., 2019). The Monte Carlo simulation program PENEPM (Llovet & Salvat, 2017) has the advantage over other existing codes that it simulates not only the transport of primary and secondary electrons but also that of generated X-rays, thus providing the SF contribution without any further calculation. SF calculations using PENEPM (or earlier versions of it) have been validated by comparing simulation results with measurements on undiffused couples (Llovet & Galán, 2003; Fournelle et al., 2005; Llovet et al., 2012; Borisova et al., 2018) but its application to fine-grained materials has been limited (Llovet et al., 2002; Wade & Wood, 2012; Singerling & Brearley, 2018).

In this study<sup>1</sup>, we examine the influence of SF on the analysis of micron-sized mineral inclusions (radius, < 100 µm) using the Monte Carlo program PENEPM. The principal purpose of this paper is to assess the suitability of PENEPM for correcting the effect of SF in this kind of materials. We focus on the determination of Cr in olivine and serpentine inclusions hosted by chromite, and of Fe in quartz inclusions hosted by almandine garnet. Special emphasis is put on examining the influence of the boundary geometry on the accuracy of calculations.

## **2 Materials and methods**

### **2.1 Sample description**

Three samples were selected for this study. The first one (CEA-034) is an chromitite (rock composed mostly of the mineral chromite) collected from the Western Cordillera of Colombia

---

<sup>1</sup> An earlier version of this study, accepted for publication in the journal *Geochemistry*, was withdrawn by the authors because it mistakenly included some data without permission.

(Ramírez et al., 2019). The chromitite sample consists mainly of chromite grains (> 70 vol. % of chromite, Cr# [Cr/(Cr+Al), atomic ratio] = 0.57 - 0.60) and intergranular serpentine and clinocllore [(Mg)<sub>10</sub>Al<sub>2</sub>[Al<sub>2</sub>Si<sub>6</sub>O<sub>20</sub>](OH)<sub>16</sub>]. Chromite grains have sizes between 0.1 and 3 mm, with average size of 1 mm, and are strongly cracked showing pull-apart fractures. There is incipient alteration to ferrian-chromite [Fe<sup>2+</sup>(Cr,Fe<sup>3+</sup>)<sub>2</sub>O<sub>4</sub>] along cracks and rims of chromite. Chromite grains host randomly distributed silicate inclusions with sizes between 75 and 250 µm that are mainly replaced by secondary minerals serpentine and clinocllore, but some of them contain unaltered olivine up to 100 µm in radius in areas free of fissures. Some inclusions are round in shape while others display polygonal outline with rounded edges.

The second sample (CO18-24B1) corresponds to a massive chromitite of the Herbeira Massif (Cabo Ortegal, NW Spain; Moreno et al., 2001). It is mainly composed of irregular shaped chromite crystals ranging between 0.5 and 2 mm in size, and exhibiting penetrative pull-apart fractures. Intergranular minerals are mainly clinocllore and minor serpentine. The chromite grains contain abundant sub-rounded silicate inclusions (sizes from 20 to 150 µm) that have been completely serpentinized (mainly lizardite [Mg<sub>3</sub>Si<sub>2</sub>O<sub>5</sub>(OH)<sub>4</sub>] after hydration of the primary olivine, see below). Scarce Fe-Ni sulfides and platinum group mineral inclusions are also present in the chromite grains. The chromite is Cr-rich, with Cr# between 0.80 and 0.82 and presents homogeneous composition across the grains. Only locally, thin rims (~2 µm) of porous magnetite (Fe<sub>3</sub>O<sub>4</sub>) can be observed overgrowing some chromite grains.

The third selected sample (ARG-16) is composed by grains of quartz up to 100 µm in diameter included in almandine garnet associated with rocks of garnet-mica schist (which are mainly formed by muscovite mica [KAl<sub>2</sub>(AlSi<sub>3</sub>O<sub>10</sub>)(OH)<sub>2</sub>], quartz and garnet) from the Mazarrón area (Murcia, SE Spain). This almandine was formed by regional metamorphism that affected Paleozoic detrital materials of the Nevado-Filábride complex, which is the bottom unit of the Internal Zone of Betic ranges (Gómez-Pugnaire and Franz, 1988; Vera, 1988). During their growth, precursor detrital quartz was trapped generating grains of almandine with typical quartz inclusions.

## 2.2 Electron microprobe measurements

EPMA measurements were performed using a JEOL JXA-8230 electron microprobe at the Scientific and Technological Centers at the University of Barcelona. Analyses were conducted using a 20 kV accelerating voltage and 15 to 100 nA beam current with a 1 µm spot size. Measured elements were counted for 10 s on peak and 10 s on background, on each side of the peak, with the exception of Cr (in olivine and serpentine) and Fe (in quartz), for which count times were 60 s on peak and 60 s on background. A range of silicate and oxide standards, measured under the same analytical conditions as the samples, were used to convert X-ray intensities into concentrations using the XPP matrix correction method (Pouchou & Pichoir, 1991). Cr and Fe were measured

using PETL and LiFH analyzing crystals, respectively. The analytical precision of the measured Cr and Fe contents, as expected from counting statistics, was ~ 3 - 4% (at 1 $\sigma$  level). The detection limit (at 3 $\sigma$  level) of Cr in olivine and serpentine and of Fe in quartz was ~100 - 120 ppm.

For each analyzed sample, between 10 - 15 mono-phase inclusions were selected such that the compositional variation of major elements was less than ~1 wt.%. Spot analyses were collected on the center of the inclusions and at around 10 - 20  $\mu$ m from the interface on the corresponding matrices. Backscattered electron (BSE) images were collected for each analyzed inclusion.

A Cr concentration profile was also measured by stage scanning along a line profile from core to rim on a big olivine inclusion. The traverse direction was selected such that it ran approximately along the focal line of the spectrometer in an attempt to minimize spectrometer defocusing of the fluorescence intensity away from the focal line (Kronz et al., 2012; Buse et al., 2018). The focal line of the spectrometer was estimated from a beam scan X-ray map collected on a Cr<sub>2</sub>O<sub>3</sub> standard.

### 2.3 Secondary fluorescence calculations

In EPMA, quantitative analysis is performed by measuring the ratio of the characteristic X-ray intensity  $I$  emitted by an element in the specimen to that emitted by the same element in a reference material (standard). This ratio is usually referred to as the  $k$ -ratio. The relative elemental concentration  $c$  is then obtained by solving the quantification equation

$$k = \frac{I}{I^{\text{std}}} = \frac{c}{c^{\text{std}}} Z A F, \quad (1)$$

where  $c^{\text{std}}$  is the element's concentration in the standard,  $I^{\text{std}}$  is the X-ray intensity emitted from the standard, and ZAF is the matrix correction factor. The latter factor takes into account the differences in matrix effects between sample and standard (Reed, 2005). It is worth pointing out that matrix corrections are computed assuming that both sample and standards are chemically uniform.

Considering a sample consisting of two adjacent materials A and B (e.g., an undiffused couple or an inclusion in a matrix), and splitting the X-ray intensity into primary ( $I_p$ ) and fluorescence ( $I_F$ ) contributions, the apparent  $k$ -ratio due to SF  $k_F(d)$  can be obtained as

$$k_F(d) = \frac{I_F(d)}{I^{\text{std}}}, \quad (2)$$

where we have assumed that i) the beam impacts on material A at a distance  $d$  from the interface, ii) the element of interest is not present in material A, i.e.,  $I_p = 0$  and iii) all fluorescence X-rays emerging in the direction of the spectrometer are recorded, regardless of the position from where they are emitted. The apparent concentration due to SF can then be obtained by substituting  $k_F(d)$  for  $k$  in Eq. (1).

Apparent  $k$ -ratios  $k_F(d)$  were calculated using the program PENEPM (Llovet & Salvat, 2017). This program performs Monte Carlo simulations of EPMA measurements and provides the intensities of X-rays emitted at a specific direction, splitted into the different components (primary X-rays, characteristic fluorescence and continuum fluorescence). PENEPM also allows visualization of the spatial distribution of X-ray emission by recording, inside a pre-selected sample volume, the coordinates from where X-rays are emitted. PENEPM uses the subroutine package PENELOPE (Salvat, 2015), which simulates electrons, photons and positrons in matter in the energy range 50 eV to 1 GeV. A geometry package allows simulating targets consisting of homogeneous “bodies” limited by quadric surfaces, whose shape is defined in terms of quadratic equations.

In PENEPM, photon trajectories are simulated interaction by interaction (detailed mode). In contrast, electron trajectories are simulated by using an algorithm which combines detailed simulation of interactions with large angular deflections and energy losses with “condensed” simulation of interactions with small deflections and energy losses. The simulation algorithm is specified by means of several parameters; tuning these parameters adequately can greatly improve the efficiency of the simulation (Llovet & Salvat, 2018). Simulations can be further optimized by forcing selected interactions using variance-reduction techniques. To set up a simulation using PENEPM, the user must specify not only the parameters that characterize their experiment (e.g., electron beam energy, sample composition and geometry, detector aperture and take-off angle, etc.), but also the simulation and forcing parameters. A summary of the simulation of forcing parameters used in this work is given in Table 1 (for a detailed explanation see Salvat (2015)).

Apparent SF intensities  $I_F(d)$  were simulated for olivine and serpentine as inclusions hosted by chromite and for quartz as inclusions hosted by almandine garnet using compositions obtained from EPMA results (Table 2). For convenience, the olivine and serpentine inclusions were assumed to be Cr-free. Likewise, quartz inclusions were assumed to be Fe-free. In the case of serpentine, the difference to 100% of the total of the EPMA analyses was assumed to be water. The inclusions were first modelled as hemispheres with radius  $r_a$  ranging from 5 to 100  $\mu\text{m}$ , and the beam was set to impact on the hemisphere center (Fig. 1a). In one of the inclusions (olivine inclusion of 85.7  $\mu\text{m}$  radius), apparent intensities were simulated for electron beams impacting along a line profile from core to rim. In this case, simulations were also performed for an undiffused olivine-chromite couple, for electron beams impacting at different distances from the boundary (Fig. 1b). To obtain  $I^{\text{std}}$  (Eq. (2)), simulations were performed for bulk  $\text{Cr}_2\text{O}_3$  and  $\text{Fe}_2\text{O}_3$  samples (reference standards). To obtain the apparent concentrations, the apparent  $k$ -ratios were corrected for matrix effects using the XPP model (Pouchou & Pichoir, 1991). Annular ( $360^\circ$ ) and semi-annular detectors ( $180^\circ$ ) with a latitudinal angular opening of  $10^\circ$  centered on a  $40^\circ$  take-off angle were simulated.

Apparent  $k$ -ratios were also obtained for truncated spheres having the same apparent radius  $r_a$  as the hemispheres but with different thickness  $t$  (Fig. 1a). Two limiting cases were considered,

namely  $t = 0.58 r_a$  and  $t = 0.72 r_a$ . The former case (upper limit) would correspond to those inclusions that after the polishing procedure only one-fourth of the inclusion remains beneath the surface while in the latter case (lower limit), three-fourths of the inclusion remains in the sample. These two limiting cases are believed to provide a plausible condition of the samples.

The spatial distribution of SF X-rays was simulated for an undiffused couple and for two inclusions of radius 20  $\mu\text{m}$  and 87.5  $\mu\text{m}$ , respectively. The two adjacent minerals were olivine and chromite (sample CEA-034). In all cases, the electron beam was set to impact at 20  $\mu\text{m}$  from the boundary.

Apparent concentrations were also calculated using FANAL. This program implements a semi-analytical method for the fast calculation of SF across phase boundaries (Llovet et al., 2012). The intensities of the primary X-rays (e.g., those generated by electron impact) are obtained from short runs of a slightly adapted version of PENEPM (called PENFLUOR) for the two couple materials and the standard. Least-squares fits of the simulated intensities give the parameters of the semi-analytical expressions used in FANAL. Once these parameters have been pre-calculated for a specific material couple and a standard, FANAL computes the apparent  $k$ -ratio for a given element in the standard, electron beam distance to the interface, incident electron energy, X-ray line and take-off angle. FANAL assumes that the sample is an undiffused couple and that the spectrometer is located over the fluorescing phase, thus accounting for absorption of SF only in the fluorescing phase.

It is worth bearing in mind that both PENEPM and FANAL assume that all SF X-rays are detected regardless of the position from where they were emitted. As discussed by Buse et al. (2018), SF X-rays originating at large distances from the electron beam point of impact may not actually be detected because of their displacement with respect to the focal line of the spectrometer.

To determine the inclusion radius, each BSE image was processed with the help of the ImageJ program (<https://imagej.nih.gov/ij>) as follows. First, the measurement scale was set using the scale bar information provided by the EPMA manufacturer. After that, the image was cropped so as to select the inclusion of interest, and binarized using a contrast threshold for the purpose of classifying pixels as either background pixels or particle pixels. Because inclusions were chemically homogeneous (with a uniform gray scale) binarization by threshold provided satisfactory results. Image analysis of the thresholded image yielded the inclusion area and other parameters of interest such as the inclusion roundness, which is a measure of the curvature of the inclusion corners. Finally, the inclusion radius was calculated as the radius of the circle having the same area as that of the inclusion.

To obtain the concentrations corrected for SF effects, the apparent concentrations were interpolated at the specific inclusion radii and subtracted from the measured concentrations. Note that a rigorous SF correction would require first subtracting the apparent  $k$ -ratio from the measured

276 *k*-ratio and then correcting the resulting difference for matrix effects, with the conventional  
277 fluorescence factor *F* (in Eq. (1)) disabled.

278 The codes PENEPMMA and FANAL are freely available through the software suite  
279 CalcZAF/Standard (<http://probesoftware.com/download/CalcZAF.msi>). They are also available from  
280 the authors upon request.

281

### 282 **3 Results and discussion**

283

#### 284 **3.1 Assessment of calculations**

285 Figure 2a displays measured and calculated Cr concentrations, as a function of beam  
286 distance to the interface, for a core-to-rim traverse across an 87.5- $\mu$ m-radius olivine inclusion in  
287 chromite (sample CEA-034). The exact location of the traverse is depicted in Fig. 2b. The plotted  
288 uncertainty bars represent the statistical errors of the EPMA analyses at  $2\sigma$  level. Because the  
289 penetration range of 20 keV electrons in olivine is  $\sim 2.5$   $\mu$ m, analyses collected at less than 5  $\mu$ m  
290 from the interface were neglected to avoid the contribution from primary X-rays (i.e., those  
291 generated by electron impact). The PENEPMMA simulations shown in Fig. 2a were obtained with a  
292 semi-annular ( $180^\circ$ ) detector; this ensured that fluorescent Cr  $K\alpha$  X-rays are absorbed only in the  
293 chromite phase. The statistical errors of the simulations were less than 1%, the corresponding error  
294 bars being smaller than the symbol size.

295 The apparent Cr concentration decreases with distance to the interface, going from  $\sim 0.3$   
296 wt.% at 5  $\mu$ m from the interface to  $\sim 0.075$  wt.% at the center of the grain (i.e., at 87.5  $\mu$ m from the  
297 interface). As expected, the apparent Cr concentration is minimum at the inclusion center, which  
298 corresponds to the largest distance to the interface. The shaded area in Fig. 2a represents the  
299 uncertainty band of SF calculations, with lower and upper limits corresponding to truncated spheres  
300 with  $r_a = 87.5$   $\mu$ m and thicknesses  $t = 50.7$   $\mu$ m (lower limit) and  $t = 150.7$   $\mu$ m (upper limit),  
301 respectively (the smaller the inclusion thickness, the larger the SF enhancement).

302 The apparent concentration predicted by PENEPMMA is in good agreement with the measured  
303 profile. The small deviations observed near the inclusion boundary are attributed to a possible  
304 inclusion shape departure from that of a hemisphere and fall within the estimated uncertainty band.  
305 The good agreement between measurements and simulations is consistent with the assumption  
306 that the olivine inclusion is Cr-free. This assumption is supported by the fact that Cr is usually  
307 trivalent and thus it is not easily accepted by the olivine structure. Indeed, formation of Cr-rich  
308 olivine (Cr > 0.07 wt.%) has been mainly attributed to the presence of  $\text{Cr}^{2+}$  and requires very-high  
309 temperature or very-low oxygen fugacity (Melcher et al., 1997; Li et al., 1995; Endo, 2014),  
310 conditions that do not generally hold for terrestrial olivine such as that found in chromitites and  
311 associated peridotites (rocks containing more than 40 vol% olivine, with or without orthopyroxene

[(Mg,Fe)<sub>2</sub>Si<sub>2</sub>O<sub>6</sub>] and clinopyroxene). Alternative explanations for the formation of Cr-rich olivine inclusions such as dehydration of Cr-rich antigorite [Mg<sub>3</sub>Si<sub>2</sub>O<sub>5</sub>(OH)<sub>4</sub>] or a different Cr substitution mechanism remain not tested. Obviously, we cannot rule out the presence of Cr at trace level (< 100 ppm).

The predictions of FANAL underestimate both measured and PENEPMMA concentrations, with differences increasing with distance to the interface. At 10 μm from the interface, a ~1.5-fold underestimate is observed, while at the center of the inclusion the underestimation is by a factor of 4. The differences between the predictions of PENEPMMA and FANAL are mainly due to the different geometries assumed in the calculations, owing to the fact that both programs use essentially the same fundamental parameters. Simulations with PENEPMMA using an undiffused couple geometry closely match the predictions of FANAL (Fig. 2b) and confirm that the apparent Cr concentration decreases much faster for a plane boundary than for a hemisphere inclusion. The minor differences observed between FANAL and PENEPMMA can be partially explained by the fact that FANAL implements an isotropic emission of bremsstrahlung photons, while PENEPMMA uses a more realistic angular distribution (Acosta et al., 2002).

Because the apparent Cr concentration increases in a line profile towards the adjacent phase, the profile shown in Fig. 2a can be easily mistaken for a diffusion profile. There are examples of such kind of misinterpretation in the literature. For example, as discussed by Borisova et al. (2018), Elardo et al. (2012) measured a 60 μm wide Cr-enrichment (of up to 0.18 wt.%) in olivine adjacent to chromite, which was interpreted as Cr diffusion. Another example is the Fe concentration profiles of quartz adjacent to Fe-rich minerals presented by Müller et al. (2012), which were also interpreted as Fe diffusion without considering a likely contribution of SF.

### 3.2 Effect of boundary geometry

For a qualitative understanding of the influence of the boundary geometry, it is of interest to visualize the region from where SF X-rays are emitted. Figure 3 shows the spatial distribution of Cr K $\alpha$  X-rays for an undiffused olivine-chromite couple (Figs. 3a, 3b, 3c) and for two olivine inclusions embedded in chromite, with radius 87.5 μm (Figs. 3d, 3e, 3f) and 20 μm (Figs. 3g, 3h, 3i), respectively. In all cases, the electron beam impacts at 20 μm from the interface. The X-ray distributions correspond to X-Z planes integrated over Y (Figs. 3a, 3d, 3g), X-Y planes integrated over Z (Figs. 3b, 3e, 3h) and the X-Y plane at z = 0 μm (Figs. 3c, 3f, 3i). In the case of the 20-μm-radius inclusion, the beam position coincides with the inclusion center. Note that these spatial distributions are not corrected for absorption effects.

The distributions shown in Fig. 3 reveal that SF is generated from a relatively large chromite region. For example, in the case of the undiffused couple, fluorescence is emitted from a region ~30 μm long (X-direction), ~100 μm wide (Y-direction) and ~40 μm deep (Z-direction). The size of the

fluorescent region depends essentially on the mean free path of X-rays in olivine and chromite, which ranges from  $\sim 60 \mu\text{m}$  (for 7 keV photons) to  $\sim 600 \mu\text{m}$  (for 20 keV photons). In the case of the two inclusions, the fluorescence emitted from beneath and around the inclusions explains the much higher SF intensity observed, in comparison with that of the undiffused couple, being much larger for the smaller inclusion (Figs. 3g and 3h). Note that the distributions displayed in Figs. 3b, 3e and 3h are integrated over Z, thus the fluorescence emitted from beneath the inclusions is also revealed. Conversely, the distributions shown in Fig. 3c, 3f and 3i represent sections on the X-Y plane at  $z = 0 \mu\text{m}$ , thus they represent fluorescence emitted only at the sample surface.

### 3.3 Contributions from characteristic and bremsstrahlung photons

It is of interest to examine the contribution of characteristic and bremsstrahlung X-rays to the total fluorescence, since for simplicity the bremsstrahlung component has sometimes been neglected in SF calculations (e.g., Bastin et al., 1983).

The characteristic and bremsstrahlung contributions to the apparent  $k$ -ratio for an  $87.5\text{-}\mu\text{m}$ -radius olivine inclusion in chromite are compared in Fig. 4a. Fluorescent Cr  $K\alpha$  X-rays can only be excited by X-rays with energies higher than the Cr  $K_{III}$  absorption edge ( $E_{\text{abs}} = 5.989 \text{ keV}$ ), namely by Fe  $K\alpha$  X-rays ( $E_K = 6.404 \text{ keV}$ ) and by bremsstrahlung photons with energies higher than  $E_{\text{abs}}$ . Conversely, Mg and Si  $K\alpha$  X-rays (major elements in olivine) cannot excite Cr fluorescence. In this case, around  $\sim 83\%$  of the total fluorescence intensity is caused by bremsstrahlung photons while only  $\sim 17\%$  of the total fluorescence is caused by Fe  $K\alpha$  X-rays. If measurements were performed at 7 kV accelerating voltage (where electrons can no longer excite the Fe  $K\alpha$  line,  $E_{\text{abs}} = 7.1107 \text{ keV}$ ), SF would decrease by  $\sim 40\%$  but it would not be completely suppressed owing to the large bremsstrahlung component.

Obviously, the characteristic-to-bremsstrahlung fluorescence ratio depends on the Fe abundance in olivine. In the case of an olivine inclusion with the maximum allowed Fe contents (54.81 wt.% Fe), which corresponds to a pure fayalite composition ( $\text{Fe}_2\text{SiO}_4$ ), characteristic Fe X-rays would cause  $\sim 75\%$  of the total fluorescence, while the bremsstrahlung component would be only  $\sim 25\%$  of the total (Fig. 4b). In this case, the reduction in SF by decreasing the accelerating voltage to 7 kV would be much larger ( $\sim 75\%$ ).

### 3.4 Examples of application

In this section, three examples of application are presented to demonstrate the performance of the correction method. In two cases, the abundances of the considered elements in the inclusions are expected to be low and therefore the examples can be used as a further test of the method. BSE micrographs of selected inclusions are shown in Fig. 5. Measured and calculated apparent abundances are compared in Fig. 6, where error bars represent statistical measurement

uncertainties (at  $2\sigma$  level) and shaded areas are calculation uncertainties (see above). The uncorrected and corrected concentrations along with the average inclusion radius and roundness are listed in Table 3.

The first example concerns the analysis of Cr in olivine inclusions in chromite (sample CEA-034). Olivine is an important rock-forming mineral on Earth, being the most common phase in the upper mantle, and contains relatively small amounts of Ni, Mn, Co, Ca, Al, and Cr, which are petrogenetically of interest. As discussed earlier, the concentration of Cr in terrestrial olivine is usually low ( $< 100$  ppm) and thus the Cr contents have been mainly exploited in studies of lunar and meteorite samples. For instance, Almwark & Schmitz (2009) used the Cr contents of olivine inclusions in chromite to classify decomposed and fossil meteorites.

The apparent Cr concentration predicted by PENEPMMA ranges from  $\sim 0.6$  wt.% for inclusions of  $20\ \mu\text{m}$  radius to  $\sim 0.1$  wt.% for inclusions of  $80\ \mu\text{m}$  radius (Fig. 6a). Except for a few outliers, measured concentrations fall within the uncertainty band of calculations. The average Cr concentration is  $0.25 \pm 0.14$  wt.% and drops to  $-0.01 \pm 0.07$  wt.% after correcting for SF (Table 3), thus confirming that Cr is not present in the inclusions, at least at minor level. A residual uncertainty in the correction, arising from the lack of knowledge about the inclusion thickness, may yield negative results for very low concentrations. Thus, correcting concentrations close to the detection limit ( $\sim 0.01$  wt.%) is not expected to be reliable.

Philipps et al. (2004) measured a Cr concentration of 0.75 wt.% in an olivine inclusion in chromite from De Beers Pool diamonds (South Africa), which was exceptionally much higher than the typical Cr values found in olivine inclusions from diamonds worldwide. Rui et al. (2019) reported Cr contents of 0.05 - 0.48 wt.% in olivine inclusions hosted by chromite in chromitites from the Songshugou peridotite massif (Central China) and pointed out that such Cr values were remarkably higher than those found in interstitial olivine ( $< 0.1$  wt.% Cr). Likewise, Zaccarini et al. (2016) reported Cr concentrations of 0.32 - 0.51 wt.% in olivine inclusions hosted by chromite from chromite deposits of the Alapaevsk ophiolite (Russia), which were found to be much higher than those in interstitial olivine (0.04 - 0.12 wt.%). The latter authors pointed out that such differences were not observed for other minor elements such as Ni, Mn and Ca, which were consistently similar in both inclusions and interstitial olivine. Our results suggest that the unusual large Cr contents reported by the abovementioned authors may be mostly explained by SF enhancement. Most likely, the measured Cr abundances in olivine and pyroxene inclusions in chromite reported by Almwark & Schmitz (2009) were also affected by SF effects.

The second example concerns the determination of Fe in quartz inclusions embedded in almandine garnet (sample ARG-16). Because of its very stable configuration, quartz allows only a minimum concentration of elements in its structure, the most important being Al, Ti and Fe, which are generally found at trace level (few hundreds of ppm). Trace analysis chemistry, coupled with

cathodoluminescence, has been used to unravel the paragenesis of quartz from a variety of geological environments. The methodological details of the analysis of Al, Ti and Fe in quartz by EPMA have been reviewed by Kronz et al. (2012).

Figure 6b shows that the apparent concentration of Fe in quartz ranges from ~ 0.2 to 0.8 wt.%. Measured values fall within the uncertainty band of calculated concentrations but we note that most measured values consistently lie on or below the predictions for hemisphere inclusions (blue line). This trend, which was slightly observed in the previous example, can be reasonably expected since inclusions that are less than half buried in the original rock are more likely to fall out during sample preparation (Wade & Wood, 2012). The average measured Fe concentration is  $0.46 \pm 0.13$  wt.% and drops to  $-0.03 \pm 0.05$  wt.% after correcting for SF (Table 3), thus confirming that Fe is not present in the quartz inclusions, at least at minor level. The negative results indicate that SF has been slightly overcorrected.

Lanari et al. (2018) mapped the compositional zoning due to SF in quartz in contact with garnet and pointed out that Fe contents of quartz inclusions can be overestimated by 0.22 - 0.58 wt.% by SF. This estimation is consistent with our results for inclusions in the range ~20 - 80  $\mu$ m radius.

The last example deals with the determination of Cr in serpentine inclusions in chromite (sample CO18-24B1). Magnesian silicates such as olivine are replaced by hydrous minerals (mainly serpentine) when they react with water in a process called serpentinization (Evans et al., 2014 and references therein). Minor elements in serpentine such as Ni, Co, Cr and Sc may provide information on the serpentinization process, since these elements are inherited from the parent rock and/or introduced from external sources. For instance, serpentine inclusions with high Al and Cr contents (~0.5 wt.% Cr) from the Leka Ophiolite Complex were used to constrain the primary mineral (Plumper et al., 2012).

This example is no longer a test of the correction method since there is no a priori information on the plausible Cr contents that serpentine should contain. Figure 6c shows that most measured values are scattered above the calculated Cr concentration. The average measured concentration is  $0.37 \pm 0.11$  wt.% and drops to  $0.17 \pm 0.09$  wt.% after the SF correction (Table 3). Because the magnitude of SF depends on inclusion size, the average uncorrected concentration for inclusions with identical concentration shows a dispersion which is much larger than that expected from counting statistics. Thus, by accounting for SF effects, not only the systematic error is reduced (in this case by ~117%) but also the statistical dispersion of results (in this case by ~20%). After SF is corrected, the only uncertainty relating to systematic errors will be that of the correction itself, estimated at few hundreds of ppm.

### 3.5 Consequences for trace element analysis

The use of EPMA for trace element analysis ( $< 0.1$  wt.%) has increased over the years owing to the improved stability of electron columns operated at high-beam currents and of the development of large analyzing crystals. These developments have made it possible to routinely achieve detection limits in the range  $\sim 5 - 25$  ppm (see e.g., Cui et al., 2019). Korolyuk & Pokhilenko (2014) reported a Cr concentration of  $103 \text{ ppm} \pm 15\%$  in San Carlos olivine measured by high-current EPMA, with a detection limit of  $\sim 12$  ppm (at  $3\sigma$  level). The same olivine standard was analyzed by Batanova et al. (2015) reporting a value of  $98 \text{ ppm} \pm 5\%$  for Cr, with a detection limit of  $\sim 12$  ppm (at  $3\sigma$  level). However, because of its long-range nature, errors due to SF can much easily be overlooked for trace elements than for minor elements. This is illustrated in Fig. 7, which shows the apparent Cr concentration in olivine inclusions in chromite (sample CEA-034) as a function of inclusion radius, up to a radius of  $700 \mu\text{m}$ . For completeness, the predictions of FANAL, as a function of distance beam-interface, are also displayed. The results indicate that a contribution of  $\sim 10$  ppm Cr due to SF still affects the analysis of inclusions with radius as large as  $650 \mu\text{m}$ , which obviously is a matter of concern when analyzing for Cr at trace level. Indeed, if the Cr abundance of the inclusions were similar to that of San Carlos olivine ( $\sim 100$  ppm), the analytical error due to SF would amount to  $\sim 600\%$  when analyzing inclusions of  $100 \mu\text{m}$  radius, progressively decreasing to  $\sim 10\%$  for inclusions of  $650 \mu\text{m}$  radius. The analytical error would be less important if the sample were an undiffused couple, where a Cr enhancement of  $\sim 10$  ppm would occur at  $400 \mu\text{m}$  distance from the interface. In this case, if the Cr abundance were  $\sim 100$  ppm, the error due to SF would amount to  $\sim 32\%$  at  $100 \mu\text{m}$  and would decrease to  $\sim 10\%$  at  $400 \mu\text{m}$ . Therefore, checking on the possible analytical errors due to SF, using PENEPM or FANAL where the geometry permits, is highly advisable when analyzing at trace level because of the long-range nature of SF. Even if the boundary geometry is not accurately known, some important conclusions may still be feasible.

### Conclusions

We have shown that EPMA analyses for minor elements in micron-sized mineral inclusions are severely compromised by SF effects when the host phase contains a high abundance of the element of interest. The Monte Carlo simulation program PENEPM allows accurate modeling of electron beam measurements on mineral inclusions and yields apparent concentrations due to SF consistent with the EPMA measurements. Our methodology allows correcting SF effects and hence improving the analysis of minor constituents in mineral inclusions. Because of the long-range of SF, it is highly advisable to check on the possible analytical errors due to SF when analyzing at trace level, even if the boundary geometry is not accurately known.

### Acknowledgements

This work was partially supported by the project PID2019-105625RB-C21 granted by the Spanish Ministerio de Ciencia e Innovación to J.A.P. We thank Carlos A. Ramírez for providing the Colombia sample.

## References

- Ackerson MR, Watson EB, Tailby ND, & Spear FS** (2017) Experimental investigation into the substitution mechanisms and solubility of Ti in garnet. *Am Mineral* **102**, 158-172.
- Acosta E, Llovet X & Salvat F** (2002) Monte Carlo simulation of bremsstrahlung emission by electrons. *App Phys Lett* **80**, 3228-3230.
- Adams GE & Bishop FC** (1986) The olivine- clinopyroxene geobarometer: experimental results in the CaO-FeO-MgO-SiO<sub>2</sub> system. *Contrib Mineral Petrol* **94**, 230-237.
- Almwark C & Schmitz B** (2009) Relict silicate inclusions in extraterrestrial chromite and their use in the classification of fossil chondritic material. *Geochim Cosmochim Acta* **73**, 1472–1486.
- Bastin GF, van Loo FJJ, Vosters PJC & Vrolijk JWGA** (1983) A correction procedure for characteristic fluorescence encountered in microprobe analysis near phase boundaries. *Scanning* **5**, 172-183.
- Batanova VG, Sobolev AV, & Kuzmin DV** (2015) Trace element analysis of olivine: High precision analytical method for JEOL JXA-8230 electron probe microanalyser. *Chem Geol* **419**, 149-157.
- Brenan JM** (2003) Effects of  $f_{O_2}$ ,  $f_{S_2}$ , temperature, and melt composition on Fe-Ni exchange between olivine and sulfide liquid: Implications for natural olivine–sulfide assemblages. *Geochim Cosmochim Acta* **67**, 2663-2681.
- Borisova AY, Zagrtchenov NR, Toplis MJ, Donovan JJ, Llovet X, Asimow PD, Parseval P & Gouy S** (2018) Secondary fluorescence effects in microbeam analysis and their impacts on geospeedometry and geothermometry. *Chem Geol* **490**, 22-29.
- Buse B, Wade J, Llovet X, Kearns S & Donovan JJ** (2018) Secondary fluorescence in WDS: the role of spectrometer positioning, *Microsc Microanal* **24**, 604-611.
- Capobianco CJ & Amelin AA** (1994) Metal silicate partitioning of nickel and cobalt: The influence of temperature and oxygen fugacity. *Geochim. Cosmochim Acta* **58**, 125-140.
- Cui JQ, Yang SY, Jiang SY & Xie J** (2019) Improved Accuracy for Trace Element Analysis of Al and Ti in Quartz by Electron Probe Microanalysis. *Microsc Microanal* **25**, 47-57.
- Dalton JA & Lane SJ** (1996) Electron microprobe analysis of Ca in olivine close to grain boundaries: The problem of secondary X-ray fluorescence. *Am Mineral* **81**, 194-201.
- D’Souza RJ, Canil D & Coogan LA** (2020) Geobarometry for spinel peridotites using Ca and Al in olivine. *Contrib Mineral Petrol* **175**, 5.

527 **Elardo SM, McCubbin FM & Shearer Jr CK** (2012) The origin of chromite symplectites in lunar  
528 troctolite 76535: A new look at an old rock. In: *43rd Lunar and Planetary Science Conference*,  
529 pp. 1028.

530 **Endo S** (2014) Cr-rich olivine in deserpentinized peridotite and its implication, *Japan Geoscience*  
531 *Union Meeting*, 2014

532 **Evans BW, Hattori K & Baronnet A** (2013) Serpentinite: What, why, where? *Elements* **9**, 99–106.

533 **Feenstra A & Engi M** (1998). An experimental study of the Fe-Mn exchange between garnet and  
534 ilmenite. *Contrib Mineral Petrol* **131**, 379-392.

535 **Fournelle JH, Kim S & Perepezko JH** (2005) Monte Carlo simulation of Nb Ka secondary  
536 fluorescence in EPMA: comparison of PENELOPE simulations with experimental results. *Surf*  
537 *Interface Anal* **37**, 1012-1016.

538 **Gómez-Pugnaire MT & Franz, G** (1988). Metamorphic evolution of the Palaeozoic series of the  
539 Betic Cordilleras (Nevado-Filábride complex, SE Spain) and its relationship with the Alpine  
540 orogeny. *Geologische Rundschau* **77**, 619-640.

541 **Goodrich CA, Harlow GE, Van Orman JA, Sutton SR, Jercinovic MJ, & Mikouchi T** (2014).  
542 Petrology of chromite in ureilites: Deconvolution of primary oxidation states and secondary  
543 reduction processes. *Geochim Cosmochim Acta* **135**, 126-169.

544 **Hénoc J, Maurice F & Zemskoff A** (1969). Phenomenes de fluorescence aux limites de phases,  
545 187-192. *5th International Congress on X-ray Optics and Microanalysis*. Mollenstedt G. and  
546 Gaukler KH (Eds.) Springer-Verlag, Berlin.

547 **Hermann J, O'Neil HSC & Berry AJ** (2005). Titanium solubility in olivine in the system TiO<sub>2</sub>–MgO–  
548 SiO<sub>2</sub>: no evidence for an ultra-deep origin of Ti-bearing olivine. *Contrib Mineral Petrol* **148**,  
549 746–760

550 **Jennings ES, Wade J, Laurenz V & Petitgirard S** (2019a). Diamond anvil cell partitioning  
551 experiments for accretion and core formation: Testing the limitations of electron microprobe  
552 analysis. *Micros Microanal* **25**, 1-10.

553 **Jennings J, Wade J & Llovet X** (2019b) Comment on: “Investigating earth's formation history  
554 through copper and sulfur metal-silicate partitioning during core-mantle differentiation” by  
555 Mahan et al. (2018). *J Geophys Res-Earth* **124**, 12837-12844.

556 **Jercinovic MJ, Williams ML & Lane ED** (2008) In-situ trace element analysis of monazite and  
557 other fine-grained accessory minerals by EPMA. *Chem Geol* **254**, 197-215

558 **Jurewicz AJG & Watson EB** (1988) Cations in olivine, Part 1: Calcium partitioning and calcium-  
559 magnesium distribution between olivines and coexisting melts, with petrologic applications.  
560 *Contrib Mineral Petrol* **99**, 76-185.

561 **Köhler TP & Brey GP** (1990) Calcium exchange between olivine and clinopyroxene calibrated as  
562 a geothermobarometer for natural peridotites from 2 to 60 kb with applications. *Geochim.*  
563 *Cosmochim. Acta* **54**, 2375-2388.

564 **Kronz A, Van den Kerkhof AF & Müller A** (2012) Analysis of low element concentrations in quartz  
 565 by electron microprobe. In: *Quartz: Deposits, Mineralogy and Analytics*. Götze J and Möckel R  
 566 (Eds.) Springer-Verlag: Berlin, 191-217.

567 **Korolyuk VN & Pokhilenko LN** (2014) Electron probe determination of trace elements in olivine, X-  
 568 *ray Spectrom* **43**, 353-358

569 **Li JP, O'Neil HSC & Seifert F** (1995) Subsolidus phase relations in the system MgO–SiO<sub>2</sub>–Cr–O in  
 570 equilibrium with metallic Cr, and their significance for the petrochemistry of chromium. *J Petrol*  
 571 **36**, 107-132.

572 **Libourel G** (1999). Systematics of calcium partitioning between olivine and silicate melt:  
 573 implications for melt structure and calcium content of magmatic olivines. *Contrib Mineral Petrol*  
 574 **136**, 63-80.

575 **Lanari P, Vho A, Bovay T, Airaghi L & Centrella S** (2018) Quantitative compositional mapping of  
 576 mineral phases by electron probe micro-analyser. In: *Metamorphic Geology: Microscale to*  
 577 *Mountain Belts*. Ferrero S, Lanari P, Gonçalves P and Grosch EG (eds). Geological Society,  
 578 London, Special Publications, **478**, 39-63.

579 **Llovet X, Valovirta E & Heikinheimo E** (2000). Monte Carlo simulation of secondary fluorescence  
 580 in small particles and at phase boundaries. *Microchim Acta*. **132**, 205-212.

581 **Llovet X & Galán G** (2003) Correction of secondary X-ray fluorescence near grain boundaries in  
 582 electron microprobe analysis: Application to thermobarometry of spinel lherzolites. *Am Mineral*  
 583 **88**, 121-130.

584 **Llovet X, Pinard PT, Donovan JJ & Salvat F** (2012) Secondary fluorescence in electron probe  
 585 microanalysis of material couples. *J Phys D: App Phys* **45**, 225301.

586 **Llovet X & Salvat F** (2017) PENEPM: A Monte Carlo Program for the Simulation of X-Ray  
 587 Emission in Electron Probe Microanalysis. *Micros Microanal* **23**, 634-646.

588 **Llovet X & Salvat F** (2018). Influence of simulation parameters on the speed and accuracy of  
 589 Monte Carlo calculations using PENEPM. *IOP Conf Series: Mat Sci Eng* **304**, 012009.

590 **Longhi J, Walker D & Hays FJ** (1976). Fe and Mg in plagioclase. *Proc Lunar Sci Conf* **7**, 1281-  
 591 1300.

592 **McKay GA** (1986) Crystal/liquid partitioning of REE in basaltic systems: Extreme fractionation of  
 593 REE in olivine. *Geochim Cosmochim Acta* **50**, 69-79.

594 **Melcher F, Grum W, Grigore W, Thalhammer VT & Stumpfl EF** (1997). Petrogenesis of the  
 595 ophiolitic giant chromite deposits of Kempirsai, Kazakhstan: a study of solid and fluid inclusions  
 596 in chromite. *J Petrol* **38**, 1419-1458

597 **Moreno T, Gibbons W, Prichard HM & Lunar R** (2001) Platiniferous chromitite and the tectonic  
 598 setting of ultramafic rocks in Cabo Ortegal, NW Spain. *J Geol Soc* **158**, 601–614.

599 **Müller A, Wanvik JE & Ihlen PM** (2012) Petrological and chemical characterisation of high-purity  
600 quartz deposits with examples from Norway. In: *Quartz: Deposits, Mineralogy and Analytics*.  
601 Götze J and Möckel R (Eds.) Springer-Verlag: Berlin, 71-118.

602 **Myklebust RL & Newbury DE** (1995) Monte Carlo modeling of secondary X-ray fluorescence  
603 across phase boundaries in electron probe microanalysis. *Scanning* **17**, 235-242.

604 **Phillips D, Harris JW & Viljoen KS** (2004) Mineral chemistry and thermobarometry of inclusions  
605 from De Beers Pool diamonds, Kimberley, South Africa. *Lithos* **77**, 155-179.

606 **Plumper O, Piazzolo S & Austrheim H** (2012) Olivine pseudomorphs after serpentinized  
607 orthopyroxene record transient oceanic lithospheric mantle dehydration (Leka Ophiolite  
608 Complex, Norway). *J Petrol* **53**, 1943-1968.

609 **Pouchou JL & Pichoir F** (1991) Quantitative Analysis of Homogeneous or Stratified Microvolumes  
610 Applying the Model "PAP". In: *Electron Probe Quantitation*. Heinrich, KFJ and Newbury DE  
611 (Eds.), Plenum Press: New York.

612 **Ramírez C, Weber M, Tobón M, Proenza JA, Beltrán-Triviño A, Pujol-Solà N, Betancur S,**  
613 **Duque J & von Quadt A** (2019). Evolución tectónica desde el Jurásico superior al Mioceno en  
614 Planeta Rica, Córdoba – Aportes a la historia geológica del Caribe. *Memorias del XVII*  
615 *Congreso Colombiano de Geología*, p. 304-305.  
616 <http://sociedadcolombianadegeologia.org/Memorias/>

617 **Reed SJB & Long JVP** (1963) Electron-Probe Measurements near Phase Boundaries. In: *X-ray*  
618 *Optics and X-ray Microanalysis*. Pattee HH, Cosslett VE and Engström A (Eds.), Academic  
619 Press, 317-327.

620 **Reed SJB** (2005). *Electron microprobe analysis and scanning electron microscopy in geology*.  
621 Cambridge University Press: Cambridge.

622 **Ritchie NWM** (2017) Efficient Simulation of Secondary Fluorescence Via NIST DTSA-II Monte  
623 Carlo. *Microsc Microanal* **23**, 618-633.

624 **Robinson BW, Ware NG & Smith DGW** (1998) Modern electron-microprobe trace-element  
625 analysis in mineralogy. In: *Modern Approaches to Ore and Environmental Mineralogy*.  
626 *Mineralogical Assoc. of Canada, Short Course*. Cabri LJ and Vaughan DJ (Eds.), Vol. 27. 153-  
627 180.

628 **Rui H, Jiao J, Xia M, Yanng J & Xia Z** (2019). Origin of chromitites in the Songshugou peridotite  
629 massif, Qinling Orogen (Central China): mineralogical and geochemical evidence. *J Earth Sci*  
630 **30**, 476-493.

631 **Salvat F** (2015). *PENELOPE-2014: A code system for Monte Carlo simulation of electron and*  
632 *photon transport*. OECD/NEA Data Bank (NEA/NSC/DOC (2015)3). Retrieved from  
633 <https://www.oecd-neo.org/science/docs/2015/nsc-doc2015-3.pdf> (last access May 31, 2020)

634 **Sato K & Santosh M** (2007) Titanium in quartz as a record of ultrahigh-temperature metamorphism:  
635 the granulites of Karur, southern India. *Mineral Mag* **71**, 143-154.

636 **Singerling SA & Brearley AJ** (2018). Primary iron sulfides in CM and CR carbonaceous  
637 chondrites: Insights into nebular processes. *Meteorit Planet Sci* **53**, 2078-2106.

638 **Smith JV** (1996) X-ray emission microanalysis of rock-forming minerals II. Olivines. *J Geol* **74**, 1-16.

639 **Sugawara T** (2001). Effect of secondary fluorescence on microprobe analysis of Fa in plagioclase.  
640 *Japanese Magazine of Mineralogical and Petrological Sciences* **30**, 159-163.

641 **Vera JA** (1988) Evolución de los sistemas de depósito en el margen ibérico de las Cordilleras  
642 Béticas. *Rev Soc Geol Esp* **1**, 373-391.

643 **Wade J & Wood BJ** (2012) Metal–silicate partitioning experiments in the diamond anvil cell: A  
644 comment on potential analytical errors. *Phys Earth Planet Inter* **192–193**, 54–58.

645 **Watson EB** (1979) Calcium content of forsterite coexisting with silicate liquid in the system Na<sub>2</sub>O-  
646 CaO-MgO-ALO<sub>3</sub>-SiO<sub>2</sub>. *Am Mineral* **64**, 824-829.

647 **Yuan Y, Demers H, Rudinsky S & Gauvin R** (2019) Secondary fluorescence correction for  
648 characteristic and bremsstrahlung X-rays using Monte Carlo X-ray depth distributions  
649 applied to bulk and multilayer materials. *Micros Microanal* **25**, 92-104.

650 **Zaccarini F, Pushkarev E, Garuti G & Kazakov I** (2016) Platinum-Group Minerals and Other  
651 Accessory Phases in Chromite Deposits of the Alapaevsk Ophiolite, Central Urals, Russia.  
652 *Minerals* **6**, 108.

653 **Zhao D, Zhang Y & Essene EJ** (2015) Electron probe microanalysis and microscopy: Principles  
654 and applications in characterization of mineral inclusions in chromite from diamond deposit,  
655 *Ore Geol Rev* **65**, 733-748

656 **Zhang D, Chen Y, Mao Q, Su B, Jia LH & Guo S** (2019) Progress and challenge of electron probe  
657 microanalysis technique. *Acta Petrologica Sinica* **35**, 261-274

658 **Zhang Z, von de Handt A & Hirschmann MM** (2018) An experimental study of Fe–Ni exchange  
659 between sulfide melt and olivine at upper mantle conditions: implications for mantle sulfide  
660 compositions and phase equilibria. *Contrib Mineral Petrol* **173**, 1-19.

661

## Figure captions

Figure 1. (a) Simplified sketch showing the geometry of an inclusion.  $r_a$  = apparent radius,  $r$  = real radius,  $d$  = distance of the beam to the interface,  $t$  = inclusion thickness. (b) Cross section sketch of an undiffused couple consisting of the inclusion and matrix materials separated by a plane boundary (upper) and a hemisphere inclusion embedded in a matrix (lower). Red crosses indicate the analysis spot. When the beam impacts on the inclusion center, the distance  $d$  coincides with the apparent radius  $r_a$ .

Figure 2. (a) Measured and calculated Cr concentrations for a core-to-rim traverse in an olivine inclusion in chromite (sample CEA-034), as a function of electron beam distance to the interface. Error bars are statistical uncertainties at  $2\sigma$  level. Plusses joined by continuous lines represent PENEPMAs simulations using a hemisphere inclusion geometry. Crosses represent PENEPMAs simulations using an undiffused couple geometry. Dashed lines are FANAL results. (b) BSE image showing the olivine inclusion and the traverse location. ol = olivine, chr = chromite.

Figure 3. Simulated two-dimensional Cr  $K\alpha$  X-ray distributions in the X-Z plane integrated over Y (a, d and g), X-Y plane integrated over Z (b, e and h), and X-Y plane at  $z = 0 \mu\text{m}$  (c, f and i), for an undiffused olivine-chromite couple (upper panels), a  $87.5\text{-}\mu\text{m}$ -radius olivine hemisphere in chromite (middle panels) and an  $20\text{-}\mu\text{m}$ -radius olivine hemisphere in chromite (bottom panels). X-ray emission distributions are given in photons/cm<sup>2</sup>. In all cases the electron beam (represented by a cross in the X-Y plane and an arrow in X-Z plane) impinges on the olivine phase at  $20 \mu\text{m}$  from the boundary with chromite. Results obtained with PENEPMAs.

Figure 4. Total, characteristic and bremsstrahlung components of the apparent Cr  $k$ -ratio due to SF for an olivine inclusion (sample CEA-034) in chromite (a) and an olivine inclusion (with fayalite composition,  $\text{Fe}_2\text{SiO}_4$ ) included in the same chromite host (b). Results obtained with PENEPMAs.

Figure 5. BSE images showing selected inclusions of olivine in chromite (a,b), serpentine in chromite (c,d) and quartz in almandine garnet (e,f). ol = olivine, chr = chromite, srp = serpentine, qtz = quartz and grt = garnet.

Figure 6. Measured and calculated (PENEPMAs) Cr concentrations of olivine inclusions in chromite (a), Fe concentrations of quartz inclusions in almandine garnet (b), and Cr concentrations of

serpentine inclusions in chromite (c), as a function of inclusion radius. Error bars are statistical uncertainties at  $2\sigma$  level. See text for details.

Figure 7. Comparison between the apparent Cr concentration (in ppm) of an olivine hemisphere in chromite predicted by PENEPMMA as a function of hemisphere radius and the apparent Cr concentration predicted by FANAL as a function of distance to the interface. The horizontal line represents the detection limit of Cr in olivine that can be currently achieved by high-current EPMA. Accelerating voltage 20 kV.

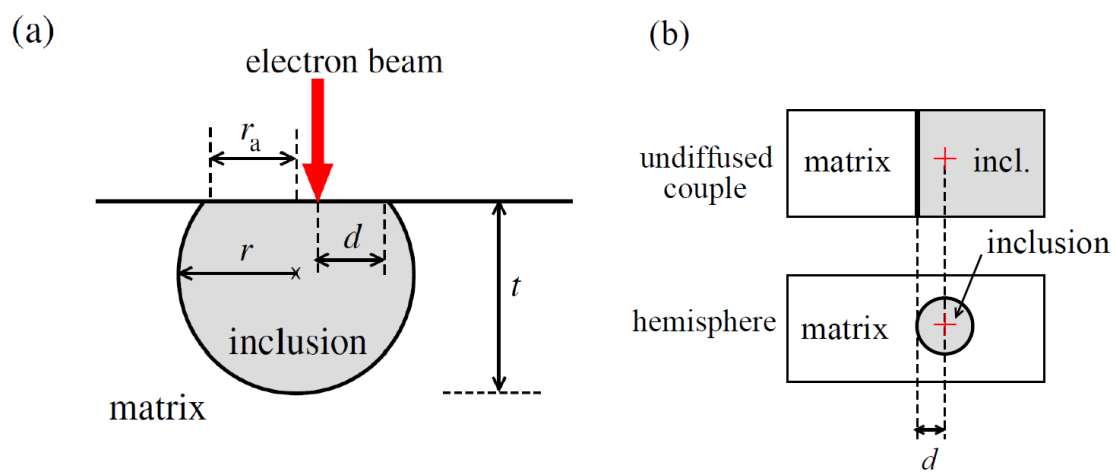


Figure 1

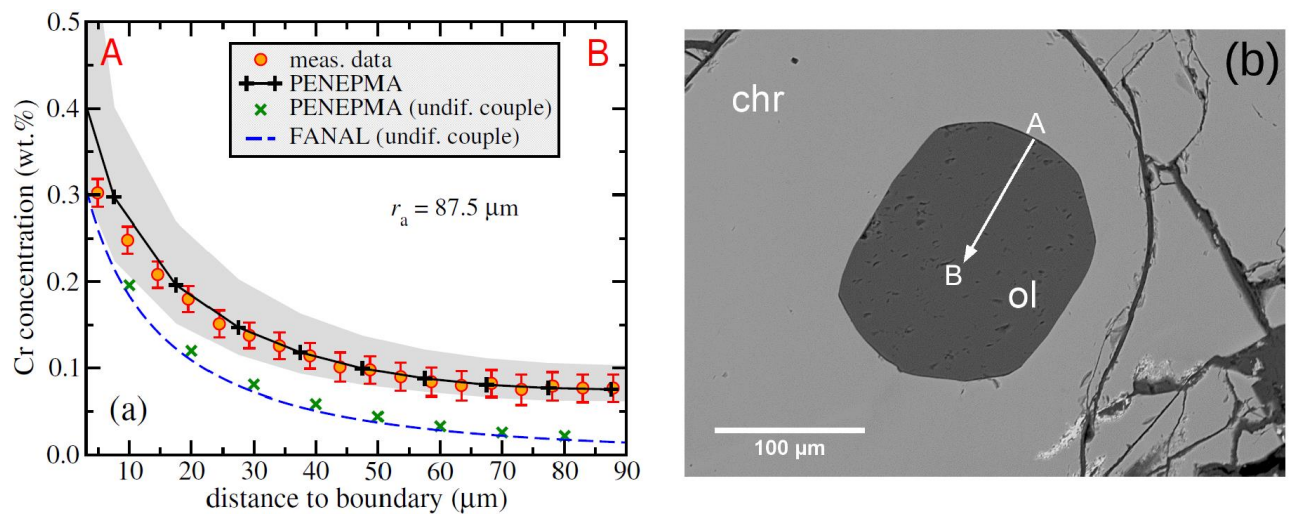
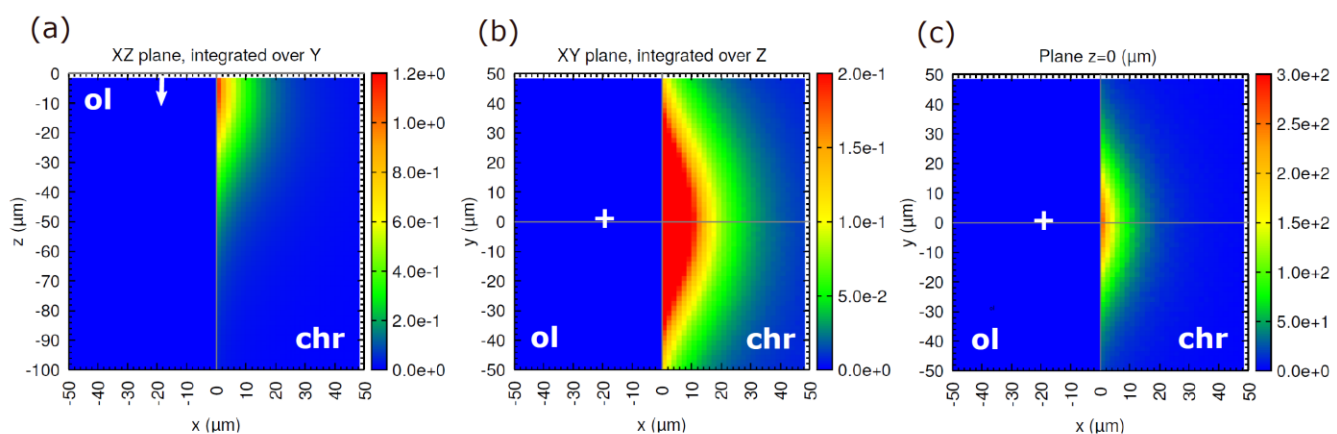
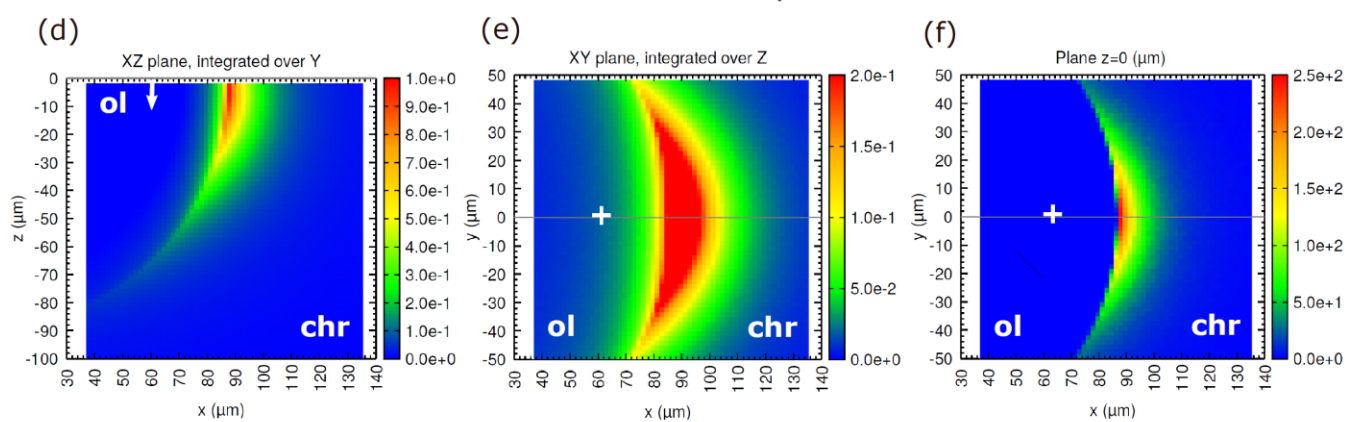


Figure 2

## Olivine-chromite couple



## Olivine inclusion 87.5 μm radius



## Olivine inclusion 20 μm radius

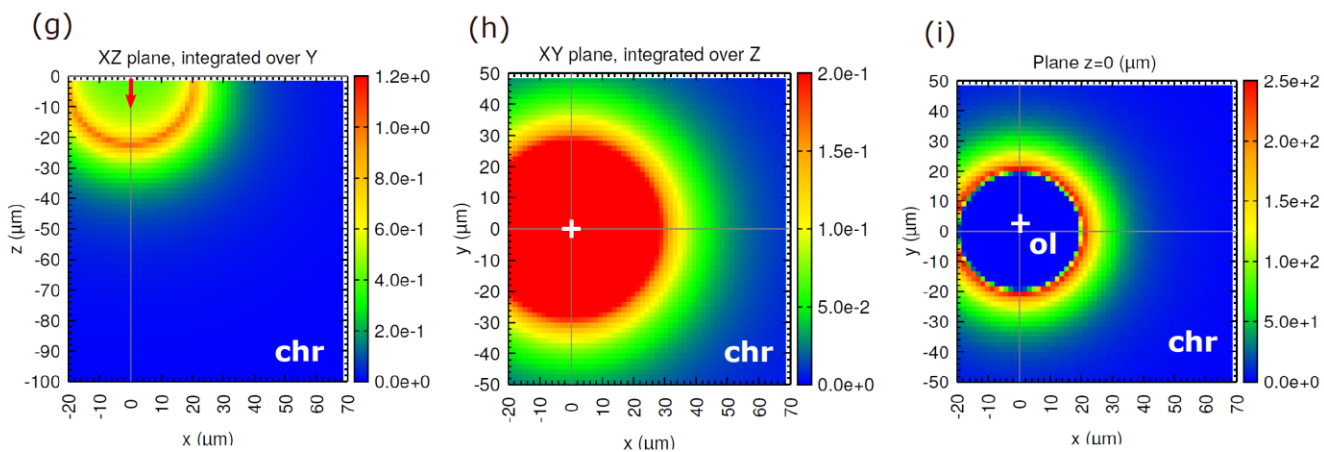


Figure 3

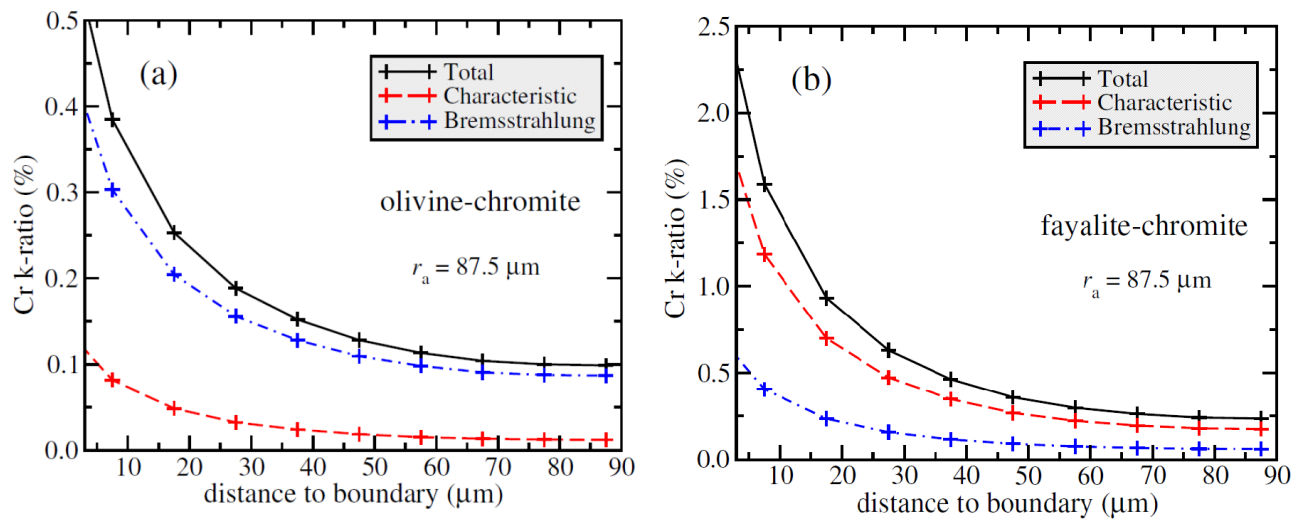


Figure 4

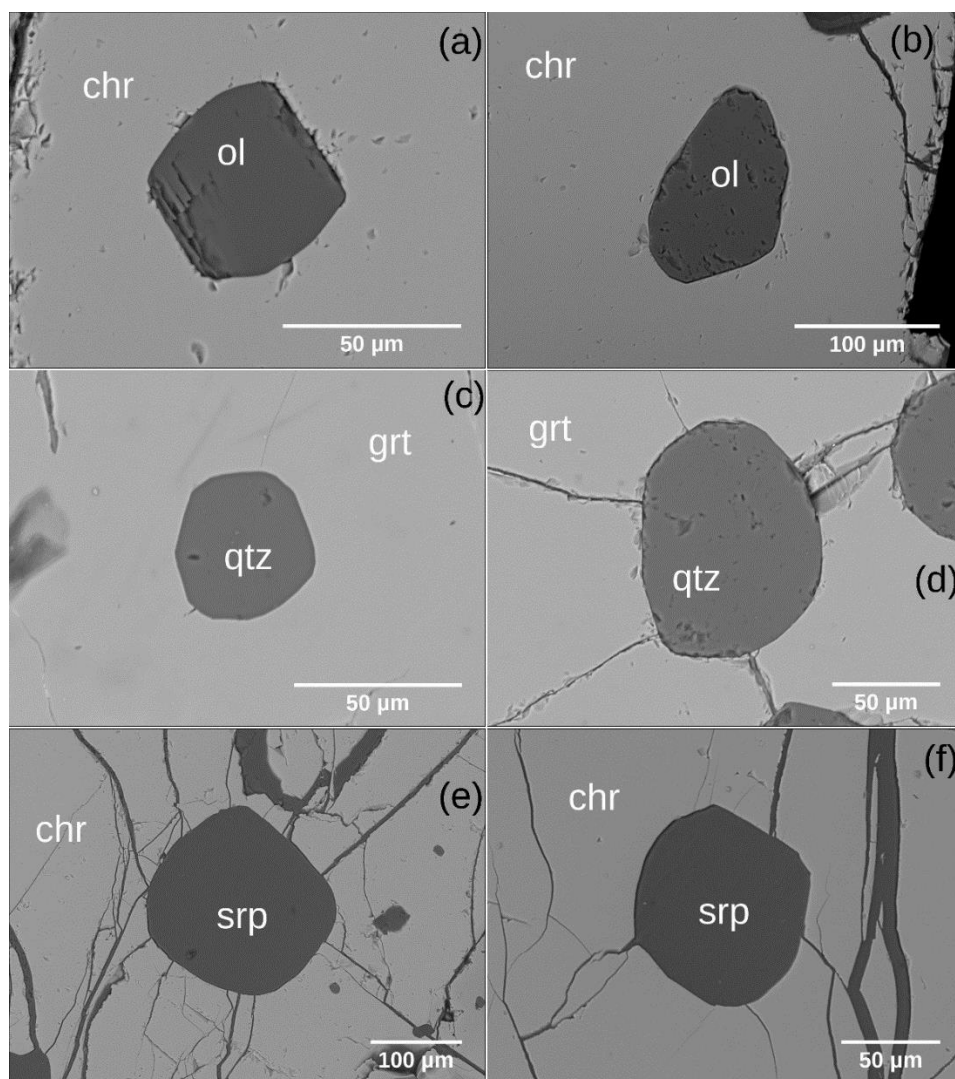


Figure 5

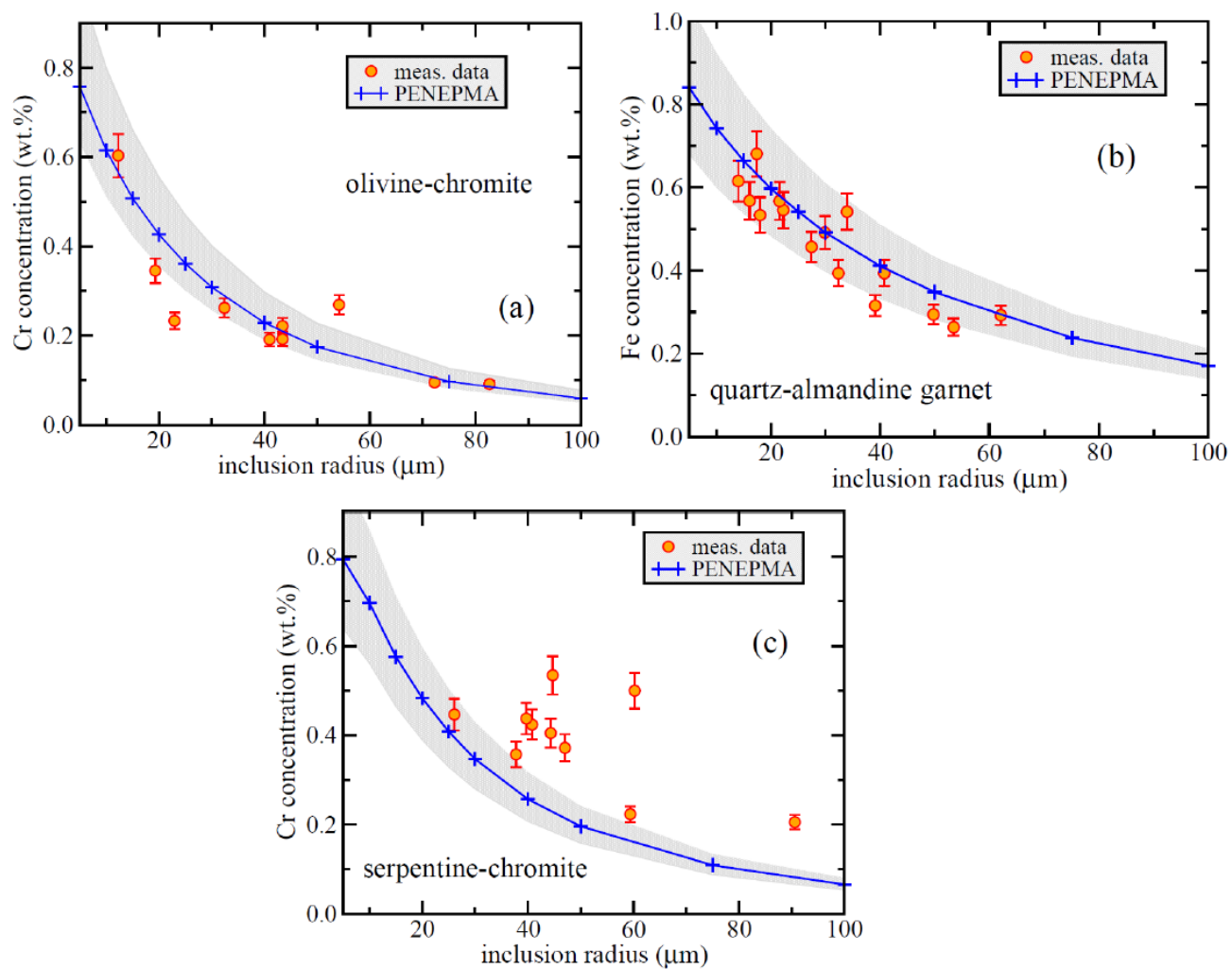


Figure 6

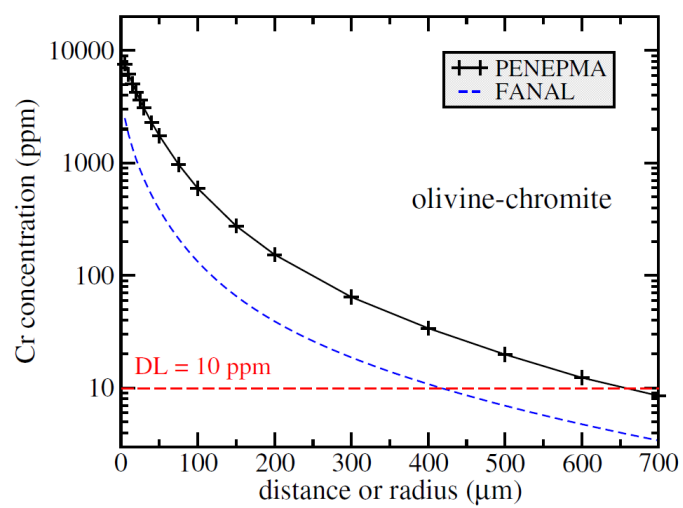


Figure 7